PHOTONICS Research

All-dielectric metasurface for fully resolving arbitrary beams on a higher-order Poincaré sphere

Hui Yang,[1] Zhenwei Xie,[1,2,4] Guanhai Li,[3] Kai Ou,[3] Feilong Yu,[3] Hairong He,[1] Hong Wang,[2] and Xiaocong Yuan[1,*]

[1]Nanophotonics Research Center, Shenzhen Key Laboratory of Microscale Optical Information Technology, Institute of Microscale Optoelectronics, Shenzhen University, Shenzhen 518060, China
[2]School of Electrical and Electronic Engineering, Nanyang Technological University, Singapore 639798, Singapore
[3]National Laboratory for Infrared Physics, Shanghai Institute of Technical Physics, Chinese Academy of Sciences, Shanghai 200083, China
[4]e-mail: ayst3_1415926@sina.com
*Corresponding author: xcyuan@szu.edu.cn

Received 1 October 2020; revised 4 January 2021; accepted 4 January 2021; posted 7 January 2021 (Doc. ID 411503); published 19 February 2021

Characterizing the amplitude, phase profile, and polarization of optical beams is critical in modern optics. With a series of cascaded optical components, one can accurately resolve the optical singularity and polarization state in traditional polarimetry systems. However, complicated optical setups and bulky configurations inevitably hinder future applications for integration. Here, we demonstrate a metadevice that fully resolves arbitrary beams on a higher-order Poincaré sphere (HOPS) via a single-layer all-silicon metasurface. The device is compact and capable of detecting optical singularities and higher-order Stokes parameters simultaneously through a single intensity measurement. To verify the validity of the proposed metadevice, different beams on $HOPS_{0,0}$ and $HOPS_{1,-1}$ are illuminated on the metadevices. The beams are fully resolved, and the reconstructed higher-order Stokes parameters show good agreement with the original ones. Taking the signal-to-noise ratio into account, the numerical simulations indicate that the design strategy can be extended to fully resolve arbitrary beams on HOPS with order up to 4. Because of the advantages of compact configuration and compatibility with current semiconductor technology, the metadevice will facilitate potential applications in information processing and optical communications.

https://doi.org/10.1364/PRJ.411503

1. INTRODUCTION

Polarization and phase are two intrinsic characteristics of electromagnetic waves, in which polarization indicates the vectorial nature of an oscillating electric field [1]. In 1892, researchers proposed a geometric representation of polarization states termed a "Poincaré sphere" (PS), which unifies all the fundamental polarizations (circular, linear, and elliptical) that exhibit spatially homogeneous distributions [2]. In such a geometric representation, the polarization states are mapped to the PS' surface through the Stokes parameters in the sphere's Cartesian coordinates. This geometric representation is a general tool for polarization-pertinent issues in numerous fields. However, the polarization states represented by a conventional PS are limited to electromagnetic waves with homogeneous polarization. For representing waves with spatially inhomogeneous polarizations (such as vector vortex beams), researchers proposed an extended generalized geometric representation known as a higher-order Poincaré sphere (HOPS) [3–8]. The HOPS incorporates spin angular momentum (SAM) and orbital angular momentum (OAM), describes the evolution of both phase and polarization, and provides a new degree of freedom for manipulating light beams. Recently, because of their intriguing properties, beams on HOPS have attracted extensive attention in optical microscopy [9,10], optical trapping [11,12], quantum information technology [13], and mode division multiplexing in optical communication [14,15].

With the development of complex optical beams and their applications, it is important to simultaneously measure the higher-order Stokes parameters and optical singularities in a compact and reliable manner. However, direct polarization measurement is unavailable because of the lack of phase information in conventional intensity probing schemes. As such, to accurately determine the polarization states in conventional methods, one must implement a series of intensity measurements via dividing the input electromagnetic waves temporally or spatially [16,17]. In particular, for characterizing

the inhomogeneous polarization state, the optical singularity associated with angular momentum must be measured as well [3]. In such measurements, complicated optical setups (such as a wave plate, polarizer, and diffractive fork gratings) and bulky configurations are inevitably introduced, hindering the development of integrated optical devices.

Metasurface, ultrathin optical components, which are capable of either replacing traditional bulky optical components or achieving exceptional functionalities, have been considered a major advancement in nano-optics [18]. The components are composed of 2D discrete meta-atoms that can locally modify the light's property and show unprecedent superiority in wavefront manipulation, thus providing an excellent platform for planar and ultracompact optical devices [19,20]. To date, researchers have demonstrated a variety of ultrathin devices based on metasurfaces, such as metalenses [21–27], vortex beam generators [6,28–30], and holograms [31–34]. Likewise, metasurface-enabled polarimeters, which accurately measure Stokes parameters in a compact configuration with straightforward setups compared with conventional counterparts have also attracted much attention [35–42]. For these devices, researchers accurately resolve the polarization states by retrieving the Stokes parameters via detecting the polarization-dependent intensity response of the metasurfaces. Despite their powerful functionalities and compact sizes, these devices are mostly limited to resolving the polarization states on standard PS. For beams on HOPSs, researchers have simultaneously detected the spin and angular momenta of these beams [43–46]. However, these devices cannot fully resolve the incident beams because they are unable to retrieve the Stokes parameters. Therefore, a compact setup capable of fully resolving beams on HOPSs is highly desirable and to date remains unexplored, to our best knowledge.

In this work, to overcome the aforementioned limitation of current polarimetry systems, we demonstrate a compact all-silicon metadevice that completely resolves arbitrary beams on HOPSs. The metadevice is composed of two main parts that detect the angular momentum and higher-order Stokes parameters, respectively. The former can be accomplished by recognizing solid spots in the helicity-decoupled focusing vortex generator, whereas the latter can be achieved by analyzing intensity contrasts in the four predesigned polarization-dependent metalenses. As a result, researchers can completely resolve incident beams on an arbitrary HOPS via a single measurement, without the need for any additional optical components.

We selected two beams of $\mathrm{HOPS}_{0,0}$ and $\mathrm{HOPS}_{1,-1}$ to verify the metadevice, and the polarization states are well reconstructed by numerical results. Our design strategy is general and can be extended to fully resolve arbitrary beams on any HOPS.

2. PRINCIPLES OF METASURFACE DESIGN

For a paraxial beam on a HOPS, the Jones vector can be expressed in a form of superposition of two circular polarization bases as

$$|\psi_{m,n}\rangle = A_R^m|R_m\rangle + A_L^n|L_n\rangle, \tag{1}$$

where

$$|R_m\rangle = \exp(im\varphi)(\hat{x} - i\sigma\hat{y})/\sqrt{2}, \tag{2}$$

$$|L_n\rangle = \exp(in\varphi)(\hat{x} + i\sigma\hat{y})/\sqrt{2}, \tag{3}$$

representing two circularly polarized vortexes with topological charges m and n, respectively. The vectors $\hat{x}$ and $\hat{y}$ represent the unit vectors along the x and y axes, respectively, and $\varphi = \arctan(y/x)$ is the azimuthal angle. Therefore, by adopting a proper set of coefficients, any point on a HOPS can be expressed as a superposition of these two circularly polarized vortexes.

For a vector vortex beam on a HOPS, the high-order Stokes parameters in the sphere's Cartesian coordinates can be derived as

$$S_0^{m,n} = |A_R^m|^2 + |A_L^n|^2, \tag{4}$$

$$S_1^{m,n} = 2|A_R^m||A_L^n|\cos\varphi, \tag{5}$$

$$S_2^{m,n} = 2|A_R^m||A_L^n|\sin\varphi, \tag{6}$$

$$S_3^{m,n} = |A_R^m|^2 - |A_L^n|^2, \tag{7}$$

where $|A_R^m|^2$ and $|A_L^m|^2$ are the intensity of $|R_m\rangle$ and $|L_n\rangle$, respectively. $\varphi = \arg(A_R^m) - \arg(A_L^n)$ is the phase difference between the two circularly polarized (CP) vortices. In particular, for the specific case $m = n = 0$, a HOPS reduces to the standard plane wave PS, and the higher-order Stokes parameters in Eqs. (4)–(7) reduce to the standard plane wave Stokes parameters. As such, to obtain a generalized description of all the beams, we treat the standard PS as a special case of HOPS in the remainder of this paper.

To fully resolve a light beam on a HOPS, three key parameters—spin of the photons σ, topological charges m and n, and higher-order Stokes parameters in Eqs. (4)–(7)—should all be resolved. The former two parameters pertain to the optical singularities, and the last parameter corresponds to the polarization states of the light beams. Figure 1(a) shows a schematic of the metasurface-based device that fully resolves the beams on a HOPS. Figure 1(a) shows an all-silicon meta-atom, from which one can see the period along the x- and y-axes P, and the height of the meta-atom h (see detailed parameters in Fig. 6 in Appendix A). To resolve the first two key parameters, we designed a CP-decoupled focusing vortex generator located in the center of the metadevice [47,48]. With the capacity to generate an independent focusing vortex for the two orthogonal circular polarizations [right-handed circularly polarized (RCP) and left-handed circularly polarized (LCP)], it discriminates the spin of the photons σ along with the topological charges m and n of the incident beam. To resolve the last key parameter, we added four elaborately designed distinctive metalenses in the four corners, with the ability to efficiently focus four predesigned polarizations [RCP, LCP, x-linearly polarized (XLP), and diagonal linearly polarized (DLP)]. By measuring the focusing efficiencies of the four metalenses and with a matrix derive calculation, one can obtain the higher-order Stokes parameters. With the three key parameters, the designed metadevice fully resolves the beams on an arbitrary HOPS. Here, we choose two common cases for $m = n = 0$ and $m = -n = 1$,

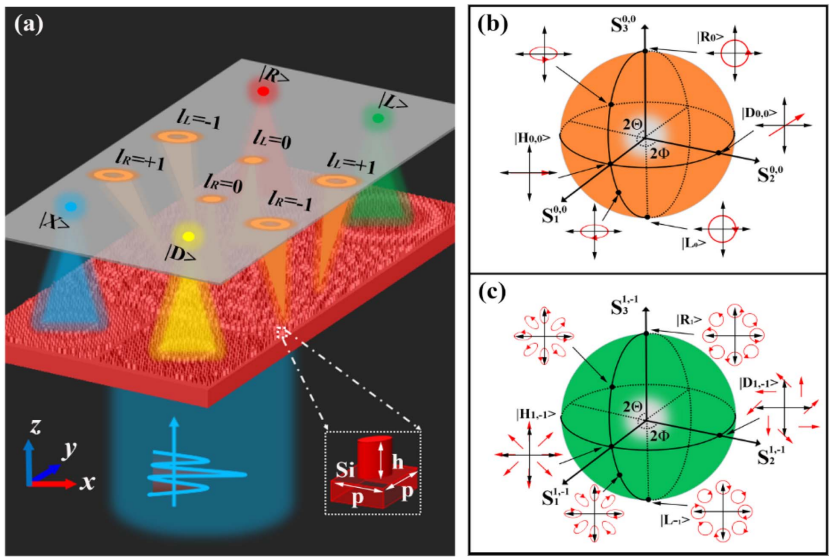

Fig. 1. (a) Schematic of the metadevice capable of fully resolving the beams on an arbitrary HOPS. Inset: Side view of the meta-atom, which consists of an all-silicon nanoblock with an elliptical cross section. The Dirac symbols $|R\rangle$, $|L\rangle$, $|X\rangle$, and $|D\rangle$ represent the focusing effects of the four predesigned metalenses for right-handed circularly polarized (RCP), left-handed circularly polarized (LCP), x-linearly polarized (XLP), and diagonal linearly polarized (DLP) light, respectively. The symbols $l_L = d$ and $l_R = d$ ($d = -1, 0, +1$) represent the generated topological charge numbers of the CP-decoupled focusing vortex generator under LCP and RCP light, respectively. One can see the period along the x- and y-axes P and the height of the meta-atom h. (b) and (c) Illustrations of the two selected HOPSs and some typical polarization state patterns on $HOPS_{0,0}$ and $HOPS_{1,-1}$, respectively.

which correspond to $HOPS_{0,0}$ (the standard plane wave PS) and $HOPS_{1,-1}$, respectively. Figures 1(b) and 1(c) show typical examples for light beam modes on two selected HOPSs. Compared with the standard PS, where the poles indicate two orthogonal CP beams (with opposite SAM), the poles of $HOPS_{1,-1}$ indicate two CP vortex beams (with different orbital angular momentum values: $m = 1$ and $n = -1$).

3. RESULTS AND DISCUSSIONS

A. Discriminating the Spin and Topological Charge of Incident Beams

To resolve the spin of photon σ as well as the topological charges m and n of the incident beam, we designed a CP-decoupled focusing vortex generator. For such a focusing vortex generator, the key issue is to obtain independent phase control under the two CPs. By accommodating both the propagation and geometric phase in the birefringent meta-atoms, one can achieve independent phase control for the two CP light beams (see detailed process in Appendix A). The phase profile $\varphi(x, y)$ of the CP decoupled focusing vortex generator can be expressed as

$$\varphi(x,y) = \arg\left\{\sum_{i=1}^{n} E_{Li}\exp[i\varphi_{Li} + il_{Li}\theta(x,y)]\right\} + \arg\left\{\sum_{i=1}^{n} E_{Ri}\exp[i\varphi_{Ri} + il_{Ri}\theta(x,y)]\right\}, \quad (8)$$

$$\varphi_{Li} = -\frac{2\pi}{\lambda}\left[\sqrt{(x-x_{Li})^2 + (y-y_{Li})^2 + f^2} - f_{Li}\right],$$
$$\varphi_{Ri} = -\frac{2\pi}{\lambda}\left[\sqrt{(x-x_{Ri})^2 + (y-y_{Ri})^2 + f^2} - f_{Ri}\right], \quad (9)$$

$$f_{Ri} = \sqrt{x_{Ri}^2 + y_{Ri}^2 + f^2}, f_{Li} = \sqrt{x_{Li}^2 + y_{Li}^2 + f^2},$$
$$\theta(x,y) = \arctan(y/x), \quad (10)$$

where E_{Li}, φ_{Li}, E_{Ri}, and φ_{Ri} are the amplitudes and phase profiles of the ith targeted light beam for LCP and RCP, respectively; l_{Li} and l_{Ri} are the topological charge number of the ith targeted focusing vortex beam for LCP and RCP, respectively; x, y are the coordinates of the meta-atoms; f is the distance from the metasurface to the focal plane; f_i is the focal length for the ith targeted focusing vortex beam; and $\theta(x, y)$ is the azimuthal angle. Here, to obtain equal energy in each channel, we assume a normalized electric field intensity $E_{Li} = E_{Ri} = (1/n)^{1/2}$.

By using Eqs. (8)–(10), we arranged the selected meta-atoms to form the CP-decoupled focusing vortex generator. The operating wavelength is $\lambda = 1.55$ μm, and the focal length is set as $f = 20$ μm. Here, we designated the CP-decoupled focusing vortex generator to generate six focusing vortexes. Three of them are for the LCP state with topological charge $l = -1, 0$, and $+1$, respectively, located at (−8 μm, 8 μm), (0 μm, 8 μm), and (8 μm, 8 μm) in the focal plane. The other three are for the RCP state with topological charge $l = +1$, 0, and −1, respectively, located at (−8 μm, −8 μm), (0 μm, −8 μm), and (8 μm, −8 μm), respectively, in the focal plane. One can decompose an arbitrary vector vortex beam on the HOPS into two orthogonal circular beams in the two poles [Eqs. (1)–(3)]. The superposition effect of the angular momentum gives a visualized method for resolving the angular momentum information because annihilation of the angular momentum ($l_{tot} = 0$) results in a solid intensity spot. Therefore, one can use the CP-decoupled focusing vortex

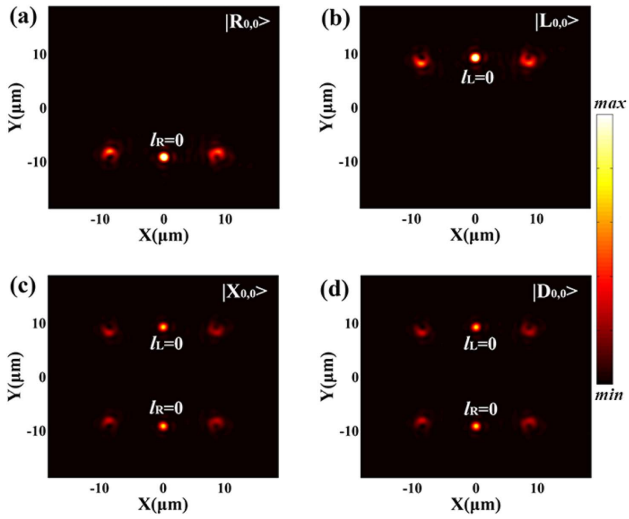

Fig. 2. Simulated intensity profiles of the CP-decoupled focusing vortex generator with four incident beams on $HOPS_{0,0}$. The four incident beams are (a) RCP, (b) LCP, (c) XLP, and (d) DLP. They are represented by Dirac symbols as $|R_{0,0}\rangle$, $|L_{0,0}\rangle$, $|X_{0,0}\rangle$, and $|D_{0,0}\rangle$, respectively.

generator to fully discriminate the spin and topological charge of the incident beam: focusing spots (when $l_{\text{tot}} = 0$) manifest at certain positions.

To demonstrate its functionality, Fig. 2 shows simulated intensity profiles of the CP decoupled focusing vortex generator under various incident light beams on $HOPS_{0,0}$. The solid spot emerges at the specific locations where total angular momentum $l_{\text{tot}} = 0$, which resolves the topological charge of the incident beams. Details of the resolving process are as follows. For convenience, we adopted a result matrix, $L_{ij} = \begin{bmatrix} -1 & 0 & +1 \\ +1 & 0 & -1 \end{bmatrix}$, to express the topological charges of the generated optical vortex, in which the first and second lines represent the topological charges of the focusing vortices generated by the LCP and RCP incident light, respectively. For the case that a solid intensity spot manifests at L_{22} [Fig. 2(a)], one can conclude that the incident beam is an RCP beam ($\sigma = -1$) with topological charge $m = 0$ (using the relationship $l_{\text{tot}} = L_{22} + m = 0$). Similarly, for the case that a solid intensity spot manifests at L_{12} [Fig. 2(b)], the incident beam can be recognized as an LCP beam ($\sigma = +1$) with topological charge $n = 0$. Otherwise, for the case that two solid intensity spots manifest at both L_{12} and L_{22} [Figs. 2(c) and 2(d)], the incident beam can be expressed as a combination of the two CP beams [Eqs. (1)–(3)], with topological charges $m = n = 0$. Similarly, for the beams on $HOPS_{1,-1}$, the topological charge can be resolved as well (see details in Appendix B). Moreover, with the same strategy, discriminating the spin and topological charge on HOPS with order up to 4 is also demonstrated (see details in Appendix B).

B. Fully Resolved Beams on $HOPS_{0,0}$ by the Designed Metadevice

To confirm the functionality of the proposed metadevice, Figs. 3(a)–3(h) show simulated intensity ($|E|^2$) profiles of the metadevice under different incident beams on $HOPS_{0,0}$. Figures 3(a)–3(d) illustrate the simulated intensity profiles of the metadevice for incident light with four polarization states on $HOPS_{0,0}$: $|R_{0,0}\rangle$, $|L_{0,0}\rangle$, $|X_{0,0}\rangle$, and $|D_{0,0}\rangle$, respectively. The simulated intensity profiles for incident light with other polarization states on $HOPS_{0,0}$ are demonstrated in Fig. 10 in Appendix B. In accordance with the previous subsection, one can resolve the topological charges of the incident beams on $HOPS_{m,n}$ as $m = n = 0$. Figures 3(e)–3(h) show the normalized intensity profiles along the x axis at $y = \pm 8$ μm in Figs. 3(a)–3(d), further confirming the correctly measured positions of the solid intensity spots. We measured the focusing

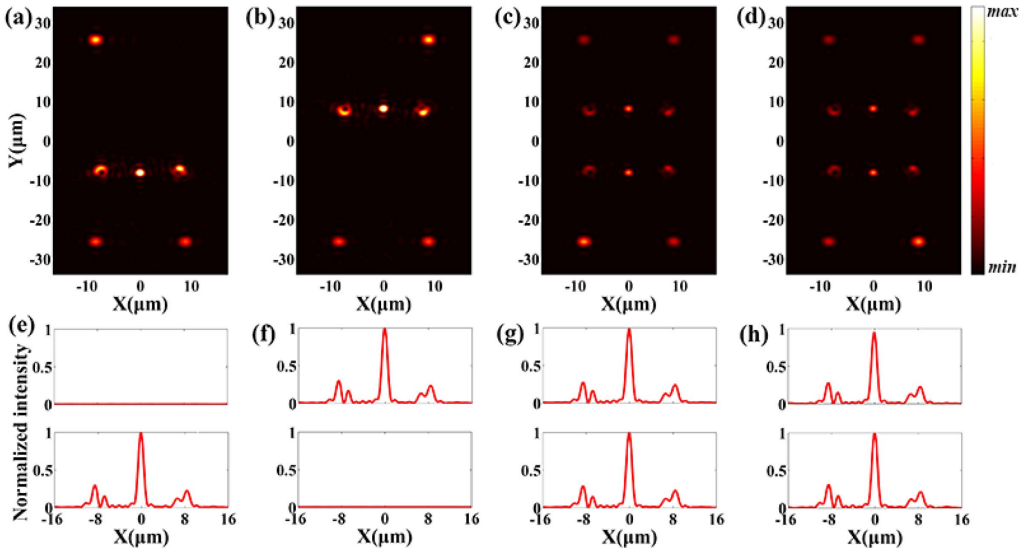

Fig. 3. Fully resolved beams on $HOPS_{0,0}$ by the designed metadevice, which is composed of a CP-decoupled focusing vortex generator and four elaborately designed distinctive metalenses. (a)–(d) Simulated intensity ($|E|^2$) profiles of the metadevice for incident light with four polarization states: $|R_{0,0}\rangle$, $|L_{0,0}\rangle$, $|X_{0,0}\rangle$, and $|D_{0,0}\rangle$, respectively. (e)–(h) Corresponding 1D cross sections of the simulated intensity profiles along the x axis at $y = \pm 8$ μm, respectively.

Table 1. Reconstructing the Stokes Parameters on $HOPS_{0,0}$ Using the Metadevice

Original Stokes Parameters $(S_0^{0,0}, S_1^{0,0}, S_2^{0,0}, S_3^{0,0})$	Simulated Intensities (%) $(I_1^{0,0}, I_2^{0,0}, I_3^{0,0}, I_4^{0,0})$	Reconstructed Stokes Parameters (Simulated)	Error
(1,0,0,1)	(5.261,0.285,3.592,3.645)	(1.0000,0.0000,0.0000,0.0000)	0
(1,0,0,−1)	(0.286,5.244,3.614,3.600)	(1.0000,0.0000,0.0000,−1.0000)	0
(1,1,0,0)	(2.661,2.643,6.248,3.576)	(1.0000,1.0000,0.0000,0.0000)	0
(1,0,1,0)	(2.574,2.961,3.569,6.410)	(1.0000,0.0000,1.0000,0.0000)	0
(1,0,−1,0)	(2.974,2.568,3.636,0.835)	(1.0002,−0.0006,−1.0002,0.0002)	0.0003
(1,−1,0,0)	(2.886,2.886,0.958,3.669)	(1.0000,−1.0000,0.0000,0.0000)	0
(1,0,0.866,0.5)	(3.844,1.695,3.568,6.048)	(0.9999,0.0001,0.8662,0.4999)	0.0001
(1,0,0.866,−0.5)	(1.356,4.175,3.579,6.025)	(0.9999,0.0001,0.8660,−0.5003)	0.0001

efficiencies of the predesigned four distinctive metalenses (located in the four corners) illuminated with different light on $HOPS_{0,0}$ (see detailed configurations in Appendix C). One can calculate the Stokes parameters of the selected incident beams by the focusing efficiency contrasts. Table 1 shows the corresponding focusing efficiencies and reconstructed Stokes parameters (see Appendix D for the detailed reconstructing process). The reconstructed Stokes parameters show good agreement with the original parameters, verifying the veracity of our metadevice. Therefore, via a single measurement, the metadevice fully resolves an arbitrary beam on $HOPS_{0,0}$.

C. Fully Resolved Beams on $HOPS_{1,-1}$ by the Designed Metadevice

Figures 4(a)–4(d) illustrate the simulated intensity profiles of the metadevice for incident light with four polarization states on $HOPS_{1,-1}$: $|R_{1,-1}\rangle$, $|L_{1,-1}\rangle$, $|X_{1,-1}\rangle$, and $|D_{1,-1}\rangle$, respectively. The simulated intensity profiles for incident light with other polarization states on $HOPS_{1,-1}$ are demonstrated in Fig. 11 in Appendix B. Similarly, by recognizing the solid intensity spots exhibited at certain positions, we successfully find the topological charges of the incident beams on $HOPS_{m,n}$ as $m = -n = 1$. Although there is a small scattered intensity field around the solid spots, one can accurately confirm the correctly measured positions of the solid spots [see the normalized intensity profiles in Figs. 4(e)–4(h)]. Moreover, Table 2 shows the corresponding focusing efficiencies and reconstructed Stokes parameters. One can reconstruct the Stokes parameters of the selected incident beams on $HOPS_{1,-1}$ by the focusing efficiency contrasts. Therefore, via a single measurement, such a metadevice also fully resolves an arbitrary beam on $HOPS_{1,-1}$.

Figure 5 shows the original (red circles) and reconstructed (blue asterisks) higher-order Stokes parameters in Tables 1 and 2. The reconstructed polarization states show good agreement with the original states for both cases, verifying the veracity of our proposed metadevice. Here, we selected incident beams on the 0- and 1-order HOPSs as examples. For our designed metadevice composed of a CP-decoupled focusing vortex generator and four elaborately designed distinctive metalenses, the simulated results indicate that the CP-decoupled focusing vortex generator can be extended to fully resolve arbitrary beams on HOPS with order up to 4 (see details in Appendix B). The four metalenses would slightly worsen the performance of the designed CP-decoupled focusing vortex generator. Considering the reported experimental results [49], the HOPS

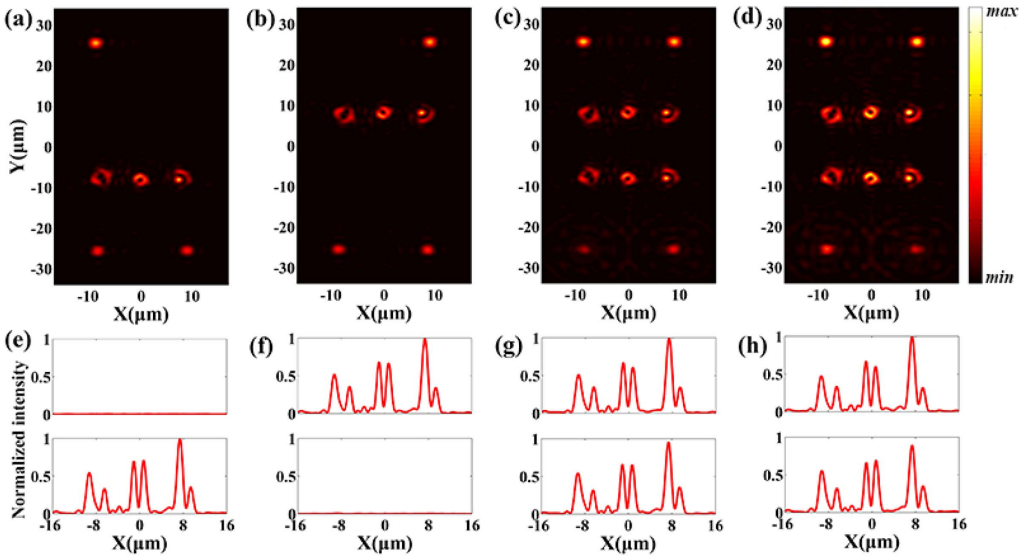

Fig. 4. Fully resolved beams on $HOPS_{1,-1}$. (a)–(d) Simulated intensity ($|E|^2$) profiles of the metadevice for incident light with four polarization states: $|R_{1,-1}\rangle$, $|L_{1,-1}\rangle$, $|X_{1,-1}\rangle$, and $|D_{1,-1}\rangle$, respectively. (e)–(h) Corresponding 1D cross sections of the simulated intensity profiles along the x axis at $y = \pm 8$ μm, respectively.

Table 2. Reconstructing the Stokes Parameters on $HOPS_{1,-1}$ Using the Metadevice

Original Stokes Parameters $(S_0^{1,-1}, S_1^{1,-1}, S_2^{1,-1}, S_3^{1,-1})$	Simulated Intensities (%) $(I_1^{1,-1}, I_2^{1,-1}, I_3^{1,-1}, I_4^{1,-1})$	Reconstructed Stokes Parameters (Simulated)	Error
(1,0,0,1)	(7.792,0.435,5.295,5.405)	(1.0000,0.0000,0.0000,0.0000)	0
(1,0,0,−1)	(0.434,7.728,5.326,5.326)	(1.0000,0.0000,0.0000,−1.0000)	0
(1,1,0,0)	(4.410,4.374,2.411,3.032)	(1.0000,1.0000,0.0000,0.0000)	0
(1,0,1,0)	(4.224,3.970,3.077,2.312)	(1.0000,0.0000,1.0000,0.0000)	0
(1,0,−1,0)	(4.002,4.193,7.543,8.420)	(0.9999,0.0013,−1.0015,0.0000)	0.0007
(1,−1,0,0)	(3.816,3.789,8.210,7.700)	(1.000,−0.9994,−0.0008,0.0000)	0.0004
(1,0,0.866,0.5)	(6.049,2.162,3.369,2.741)	(1.0001,−0.0002,0.8663,0.5000)	0.0002
(1,0,0.866,−0.5)	(2.177,6.001,7.251,7.992)	(0.9998,0.0021,0.8687,−0.4999)	0.0012

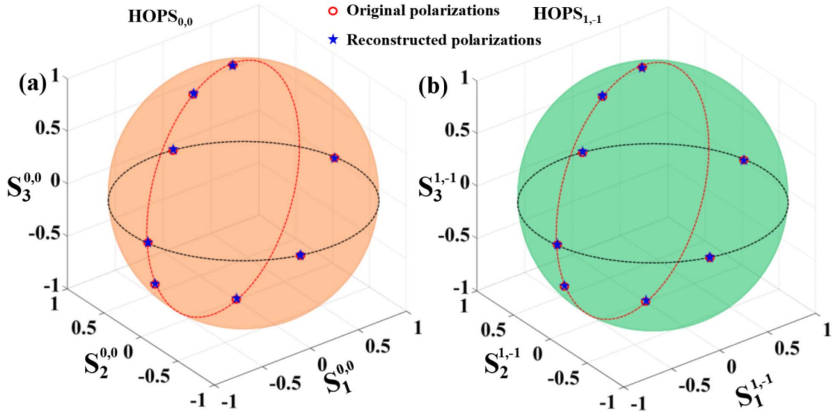

Fig. 5. Original (red circles) and reconstructed (blue asterisks) polarization states of beams on the $HOPS_{0,0}$ (orange sphere) and $HOPS_{1,-1}$ (green sphere), respectively. Here, we selected eight incident beams as examples: $|R\rangle$, $|L\rangle$, $|X\rangle$, $|Y\rangle$, $|D\rangle$, $|A\rangle$, $|EP1\rangle$, and $|EP2\rangle$. The black and red dashed lines in both HOPSs represent the latitude and longitude lines at $S_3 = 0$ and $S_2 = 0$, respectively.

with order up to 4 is not the limitation of our proposed metadevice. Hence, it is safe to say that the design strategy can be extended to fully resolve arbitrary beams on HOPS with order up to 4.

We also considered the experimental feasibility and potential applications of the proposed all-silicon metadevice. One can fabricate the single-layer all-silicon metadevice with one-step lithography and dry etching. Here, we choose an all-silicon configuration for its simpler fabrication procedure than that of the a-Si on silica substrate configuration (see Appendix E for the detailed comparison of these two configurations). The metadevice has potential applications in polarization-related information processing and optical communications. For example, orthogonally structured light beams such as optical vortex beams and cylindrical vector beams are recent candidates for high-capacity multiplexing optical communication. The metadevice would be important to this process because of its capacity to simultaneously measure the polarization states and optical singularities in a compact and reliable manner.

4. CONCLUSION

In conclusion, we proposed a compact metadevice composed of an all-silicon metasurface, which is capable of completely resolving arbitrary beams on HOPSs. Via a single measurement, one can simultaneously detect the OAM and higher-order Stokes parameters of the incident beams, without the need for additional optical components. To verify the validity of the metadevice, we selected $HOPS_{0,0}$ and $HOPS_{1,-1}$ as examples. Different beams on these two are illuminated on the metadevices, and the reconstructed polarization states show good agreement with the preset ones. Here, these two HOPSs are chosen as proof of concept, and the design strategy can be extended to fully resolve arbitrary beams on HOPS with order up to 4. Diverse applications such as polarization-related information processing and optical communications will be facilitated by the compact configuration of the metadevice and its compatibility with current semiconductor technology.

APPENDIX A: INDEPENDENT PHASE CONTROL FOR THE TWO CIRCULAR POLARIZATIONS

As demonstrated in previous works, birefringent meta-atoms with both propagation and geometric phase could achieve independent phase control of arbitrary orthogonal states of polarization [31]. To obtain independent phase control of circular polarizations, the phase relationships between the two orthogonal linear and the two orthogonal circular polarizations can be expressed as

$$\varphi_x = (\varphi_L + \varphi_R)/2, \tag{A1}$$

$$\varphi_y = (\varphi_L + \varphi_R)/2 - \pi, \tag{A2}$$

$$\theta = (\varphi_R - \varphi_L)/4, \tag{A3}$$

where φ_x, φ_y, φ_L, and φ_R are the phase shifts of x-linearly polarized (XLP), y-linearly polarized (YLP), LCP, and RCP light, respectively. Therefore, for an arbitrary set of φ_L and φ_R, one just needs to design the φ_x, φ_y, and θ according to the above equations. In other words, we can arbitrarily and independently manipulate the LCP and RCP phases by designing three parameters: the x polarized phase φ_x, the y polarized φ_y, and the rotation angle θ.

The meta-atom capable of providing independent phase control at two orthogonal linearly polarized lights (XLP and YLP) is shown in Figs. 6(a) and 6(b). The birefringent meta-atom consists of an all-silicon elliptical nanoblock (with refractive index $n = 3.47$). The detailed parameters of the meta-atom are height h, orientation angle θ, length along x-axis b, length along y-axis a, and lattice constant P. Figures 6(c)–6(f) show the transmission properties of the meta-atoms, with the simulated phase and transmission amplitude of the meta-atoms as functions of a and b for the two linear polarizations.

To achieve independent phase modulation at two orthogonal linearly polarized lights, the polarization multiplexed technology is adopted. The selected geometrical parameters of the meta-atoms that independently cover the phase coverage ($-\pi$ to π) are shown in Fig. 6. In order to obtain these optimized meta-atoms, the errors between the required and realized phase shifts as well as amplitudes are taken into consideration. The optimized geometrical parameter set (a and b) is achieved by taking minimum error value

$$\varepsilon = |t_x \cdot \exp(i\varphi_x) - \exp(i\varphi_1)| + |t_y \cdot \exp(i\varphi_y) - \exp(i\varphi_2)|, \tag{A4}$$

where t_x, φ_x, and t_y, φ_y represent the realized amplitudes and phase shifts for XLP and YLP, respectively. φ_1 and φ_2 are the objective phase shifts for XLP and YLP. By using this optimization strategy, some geometrical parameters that satisfy the desired phase shift but with low amplitude could be automatically eliminated. As shown in Fig. 7, any combination of phase shifts (ranging from $-\pi$ to π) under the two linear polarizations can be simultaneously achieved by properly choosing a set

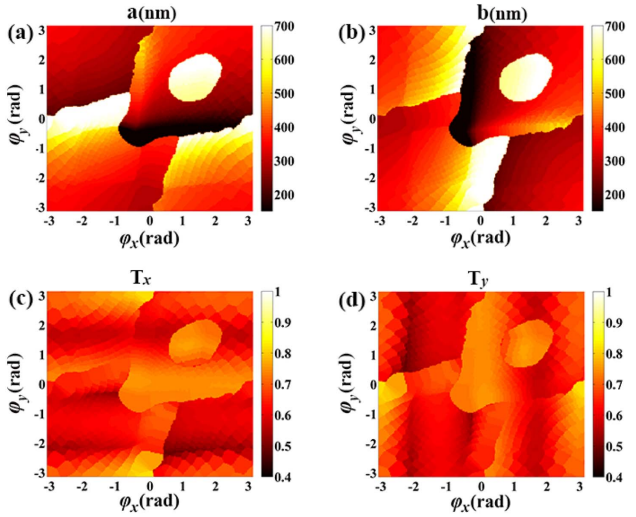

Fig. 7. Selected optimized meta-atoms. (a) and (b) Selected parameter values a and b as functions of phase shift φ_x and φ_y. (c) and (d) Transmissions for the selected meta-atoms at XLP and YLP incident lights, respectively.

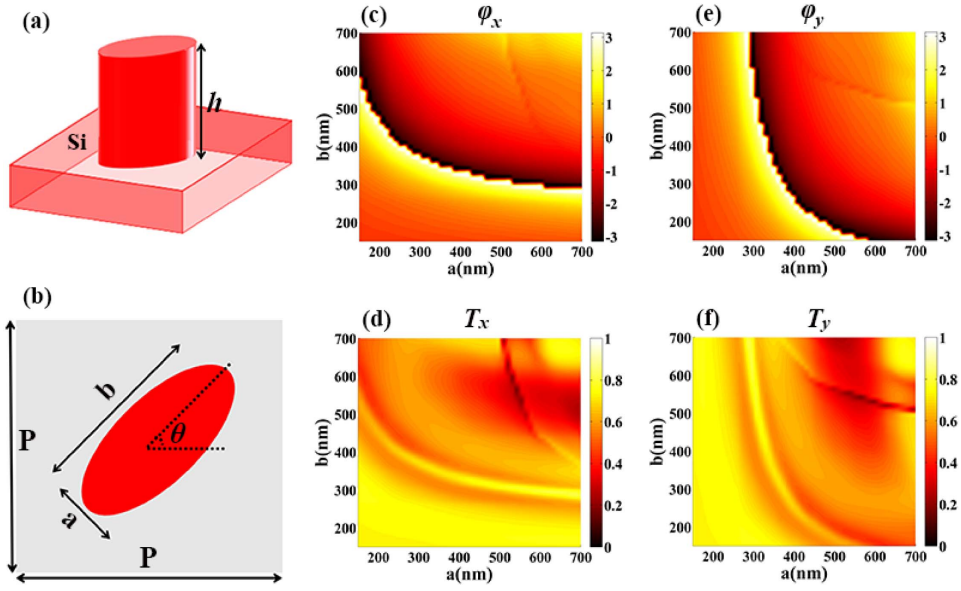

Fig. 6. (a) and (b) Side and top views of the birefringent meta-atom with elliptical cross-section, which consist of an all-silicon nanoblock. Detailed parameters of the meta-atom are the height $h = 1000$ nm, the length along x-axis a, the length along y-axis b, the lattice constant $P = 800$ nm, and the orientation angle θ. (c) and (d) Phase shift and transmission as functions of meta-atom's two lengths with x-linearly polarized (XLP) incident light. (e) and (f) Phase shift and transmission as functions of meta-atom's two lengths with y-linearly polarized (YLP) incident light. To minimize optical coupling between neighboring meta-atoms, only elliptical nanoblocks with lengths (a and b) range from 150 to 700 nm are adopted. Here, the orientation angle of the meta-atom is set as $\theta = 0$.

of geometrical parameters (a and b). Then, using the Eqs. (A1)–(A3), any arbitrary set of phase shifts φ_L and φ_R (ranging from $-\pi$ to π) can be obtained.

APPENDIX B: DISCRIMINATING THE SPIN AND TOPOLOGICAL CHARGE ON HOPS$_{m,-n}$

The simulated intensity profiles of the CP decoupled focusing vortex generator under different incident lights on HOPS$_{1,-1}$ are depicted in Fig. 8. As also depicted in Fig. 8, for the beams on HOPS$_{1,-1}$, the solid spot emerges at the specific locations where total angular momentum $l_{\text{tot}} = 0$, which is capable of resolving the topological charge of the incident beams. The detail-resolving process is as follows. Here, a result matrix L_{ij} is adopted to express the topological charges of the generated vortex beams in which the first and second lines represent the topological charges of OAMs generated by LCP and RCP incident lights, respectively. For the case that a solid intensity spot exhibits at L_{23}, one can conclude that the incident beam is an RCP beam with topological charge $m = +1$ (using the relationship $l_{\text{tot}} = L_{22} + m = 0$). Similarly, for the case that a solid intensity spot exhibits at L_{13}, the incident beam is an LCP beam with topological charge $n = -1$. Otherwise, for the case that two solid intensity spots exhibit at both L_{13} and L_{23}, the incident beam can be expressed as a combination of the two circularly polarized beams as expressed in Eqs. (1)–(3) in the main text, with topological charges $m = -n = 1$. Therefore, the designed CP decoupled focusing vortex generator is able to simultaneously resolve the spin of photon and topological charges of the incident beam on HOPS$_{1,-1}$.

Moreover, with the same design strategy, discriminating the spin and topological charge on HOPS with order up to 4 is also demonstrated. By using Eqs. (8)–(10), we arranged the selected meta-atoms to form the required CP-decoupled focusing vortex generator. The operating wavelength is $\lambda = 1.55$ μm, and the focal length is set as $f = 40$ μm. Here, we designated the

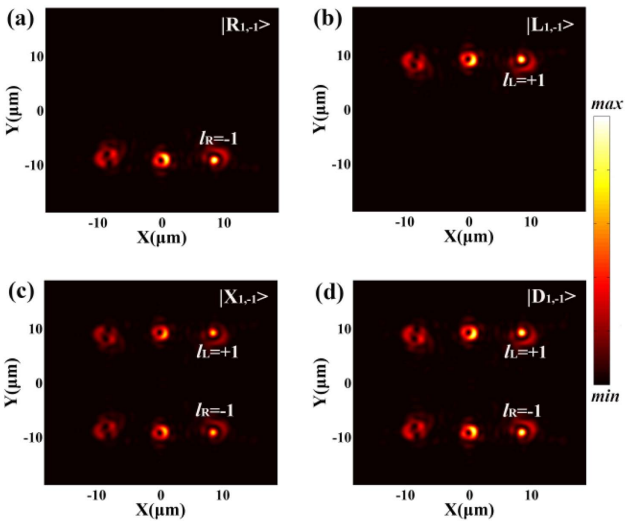

Fig. 8. Simulated intensity profiles of the CP decoupled focusing vortex generator with incident beams on HOPS$_{1,-1}$. Four incident beams are selected as examples: (a) RCP, (b) LCP, (c) XLP, (d) DLP, and their Jones vectors are represented as $|R_{1,-1}\rangle$, $|L_{1,-1}\rangle$, $|X_{1,-1}\rangle$, $|D_{1,-1}\rangle$, respectively.

CP-decoupled focusing vortex generator to generate 18 focusing vortexes. Nine of them for the LCP state with topological charge $l = -4$ to $+4$, respectively, are located at (6 μm, −20 μm), (6 μm, −10 μm), (6 μm, 0 μm), (6 μm, 10 μm), (6 μm, 20 μm), (18 μm, 10 μm), (18 μm, 0 μm), (18 μm, −10 μm), and (18 μm, −20 μm) in the focal plane. The other nine are for the RCP state with topological charge $l = +4$ to −4, respectively, located at (−6 μm, −20 μm), (−6 μm, −10 μm), (−6 μm, 0 μm), (−6 μm, 10 μm), (−6 μm, 20 μm), (−18 μm, 10 μm), (−18 μm, 0 μm), (−18 μm, −10 μm), and (−18 μm, −20 μm) in the focal plane. For convenience, a matrix P is adopted to express the appointed topological charges of the CP-decoupled focusing vortex generator as

$$P = \begin{bmatrix} 4 & 3 & 2 & 1 & \times \\ -4 & -3 & -2 & -1 & 0 \\ 4 & 3 & 2 & 1 & 0 \\ -4 & -3 & -2 & -1 & \times \end{bmatrix}, \tag{B1}$$

where the upper two lines and lower two lines represent the topological charges of the focusing vortexes generated by the LCP and RCP incident light, respectively. The simulated intensity profiles of the CP-decoupled focusing vortex generator with incident beams on different HOPS$_{m,n}$ are shown in Fig. 9. It can be observed that the solid spot emerges at the specific locations where total angular momentum $l_{\text{tot}} = 0$, which resolves the topological charges of the incident beams. The topological charges of the selected specific HOPSs in Figs. 9(a)–9(f) can be resolved as $m = 4$, $n = -4$, $m = 2$, $n = -2$, $m = 0$, $n = 0$, $m = 3$, $n = -3$, $m = -2$, $n = -4$, $m = 1$, and $n = -3$, respectively. Here, the HOPS with order up to 4 is selected due to limitations of the computing capacity of our work station.

APPENDIX C: DETAILED CONFIGURATION OF THE FOUR PREDESIGNED METALENSES

The P-B phase is introduced to the design of the two metalenses for focusing the LCP and RCP incident lights. To fulfill the P-B phase condition, the meta-atom is optimized to function as a half-wave plate, and the polarization conversion rate is also optimized as unity at the working wavelength. The corresponding parameters of the all-silicon meta-atom are $a = 200$ nm, $b = 480$ nm, and $h = 1000$ nm. The polarization conversion rate of the meta-atom as a function of the incidence wavelength is depicted in Fig. 12(a). The polarization conversion rate over 99% at 1550 nm indicates the half-wave plate functionality of the meta-atom. In this condition, the meta-atom is able to flip the helicity of the input circularly polarized light and to impart an additional phase shift of 2θ on the output light. The phase shift of the meta-atom as a function of rotation angles θ is plotted in Fig. 12(b). It is obvious that the phase shift and the rotation angle satisfy the P–B phase condition ($\varphi = 2\theta$).

For the metalens designed for XLP incident light, the meta-atoms are selected from Figs. 7(c) and 7(d) with minimum error value, where φ_x and φ_y are the desired and object phase shifts for XLP incident light. Moreover, rotating all the meta-atoms of the metalens for XLP incident light with an

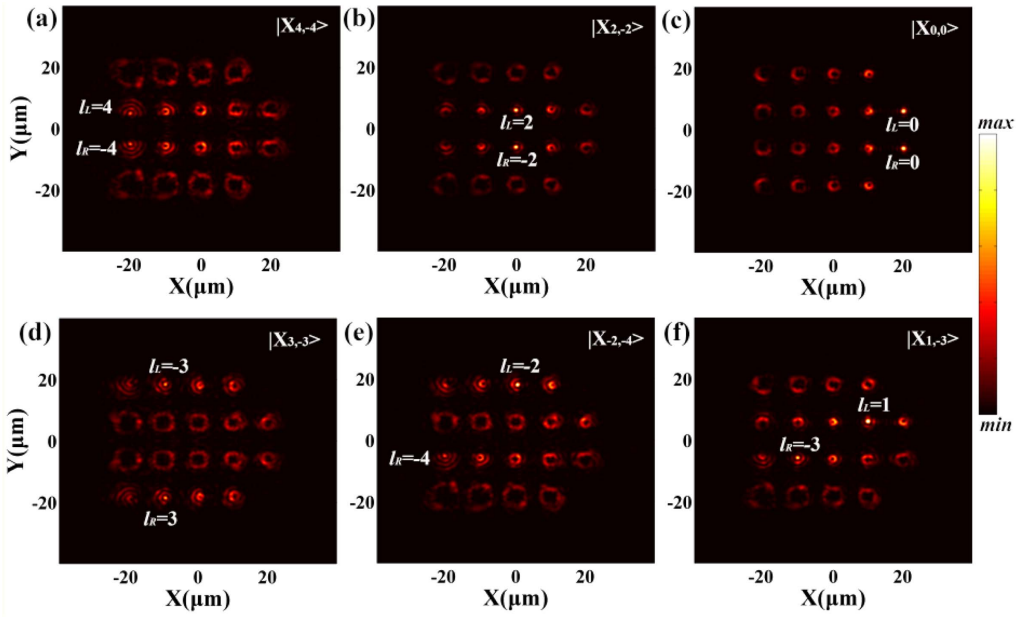

Fig. 9. Simulated intensity profiles of the CP-decoupled focusing vortex generator with incident beams on different $HOPS_{m,n}$. Incident XLP beams on specific $HOPS_{m,n}$ are selected as examples, and their Jones vectors are represented as $|X_{4,-4}\rangle$, $|X_{2,-2}\rangle$, $|X_{0,0}\rangle$, $|X_{-3,3}\rangle$, $|X_{-2,-4}\rangle$, and $|X_{1,-3}\rangle$, respectively.

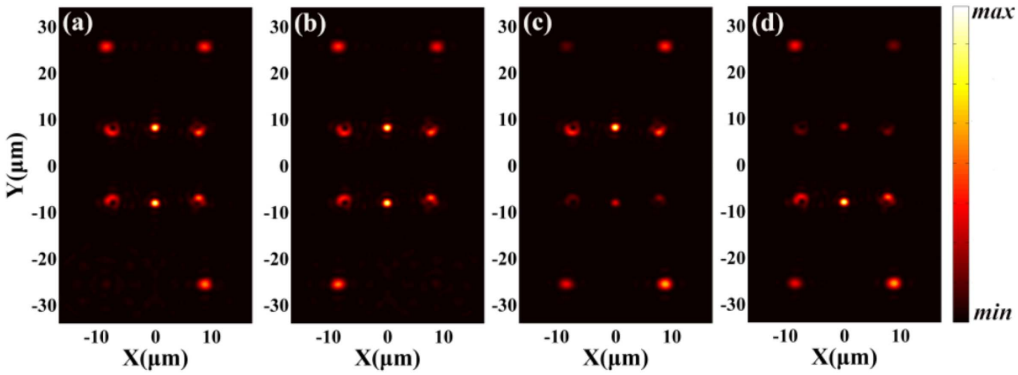

Fig. 10. Intensity ($|E|^2$) profiles of the metadevice for incident lights on $HOPS_{0,0}$ with four different polarization states: (a) *y*-linearly polarized (YLP); (b) antidiagonal linearly polarized (ALP); (c) elliptically polarized (EP1) with ellipticity +0.5; (d) elliptically polarized (EP2) with ellipticity −0.5.

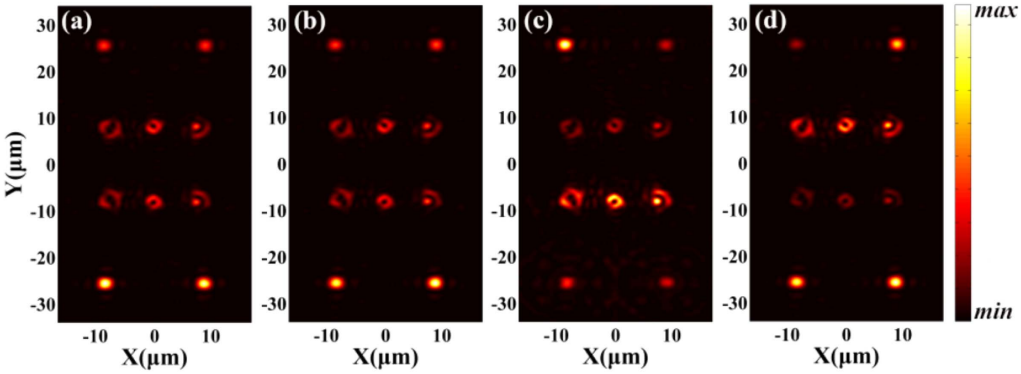

Fig. 11. Intensity ($|E|^2$) profiles of the metadevice for incident light on $HOPS_{1,-1}$ with four different vector lights situated at the same locations as those in Fig. 9: (a) *y*-linearly polarized (YLP, $|Y_{1,-1}\rangle$); (b) antidiagonal linearly polarized (ALP, $|A_{1,-1}\rangle$); (c) elliptically polarized ($|EP1_{1,-1}\rangle$) with ellipticity +0.5; (d) elliptically polarized ($|EP2_{1,-1}\rangle$) with ellipticity −0.5.

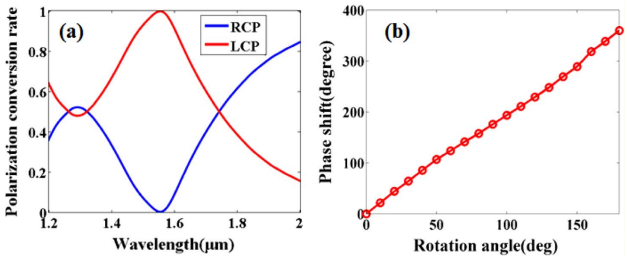

Fig. 12. (a) Polarization conversion rate of the optimized meta-atom versus incident wavelength. The red and green lines represent the ratio of the LCP and RCP components to the total transmission, respectively. (b) Phase shift of the optimized meta-atom versus rotation angle θ.

angle of 45°, the metalens designed for DLP incident light is achieved.

APPENDIX D: CALCULATING THE HIGHER-ORDER STOKES PARAMETERS

For the vector vortex beam on HOPS, the higher-order Stokes parameters in the sphere's Cartesian coordinates can be derived as

$$S_0^{m,n} = |A_R^m|^2 + |A_L^n|^2 \propto I, \tag{D1}$$

$$S_1^{m,n} = 2|A_R^m||A_L^n|\cos\varphi = |A_X^{m,n}|^2 - |A_Y^{m,n}|^2, \tag{D2}$$

$$S_2^{m,n} = 2|A_R^m||A_L^n|\sin\varphi = |A_D^{m,n}|^2 - |A_A^{m,n}|^2, \tag{D3}$$

$$S_3^{m,n} = |A_R^m|^2 - |A_L^n|^2, \tag{D4}$$

where $|A_R^m|^2$ and $|A_L^n|^2$ are the intensity of $|R_m\rangle$ and $|L_n\rangle$, respectively. $\varphi = \arg(A_R^m) - \arg(A_L^n)$ is the phase difference between the two circular polarizations. It is clear that the first higher-order Stokes parameter $S_0^{m,n}$ is proportional to the intensity of incident beam I, whereas $S_1^{m,n}$–$S_3^{m,n}$ describe the states of polarization. The latter three Stokes parameters can be obtained by respectively measuring the intensities of the three orthonormal polarization basis (x, y), (d, a), and (r, l). Here, the diagonal and antidiagonal polarization basis (d, a) corresponds to a rotation of the coordinate system (x, y) by ±45° with respect to the x axis. From the above description of Stokes parameters, it is clear that six polarization components need to be measured to uniquely determine the higher-order Stokes parameters. To simplify the measuring process, a set of four intensity components $(I_R^m, I_L^n, I_X^{m,n}, I_D^{m,n}) = (|A_R^m|^2, |A_L^n|^2, |A_X^{m,n}|^2, |A_D^{m,n}|^2)$ is introduced, which are capable of determining the Stokes parameters as well. The four intensity components can be derived from Eqs. (D1)–(D4) as

$$I_R^m = |A_R^m|^2, \tag{D5}$$

$$I_L^n = |A_L^n|^2, \tag{D6}$$

$$I_X^{m,n} = \frac{1}{2}(|A_R^m|^2 + |A_L^n|^2 + 2A_R^m A_L^n \cos\varphi), \tag{D7}$$

$$I_D^{m,n} = \frac{1}{2}(|A_R^m|^2 + |A_L^n|^2 + 2A_R^m A_L^n \sin\varphi). \tag{D8}$$

From Eqs. (D1)–(D9), there is a linear relationship among the four intensity components $(I_R^m, I_L^n, I_X^{m,n}, I_D^{m,n})$ and the higher-order Stokes parameters, which can be described by a 4×4 device matrix $M^{m,n}$ as

$$\begin{pmatrix} S_0^{m,n} \\ S_1^{m,n} \\ S_2^{m,n} \\ S_3^{m,n} \end{pmatrix} = M^{m,n} \cdot \begin{pmatrix} I_R^m \\ I_L^n \\ I_X^{m,n} \\ I_D^{m,n} \end{pmatrix} = \begin{pmatrix} 1 & 1 & 0 & 0 \\ -1 & -1 & 2 & 0 \\ -1 & -1 & 0 & 2 \\ 1 & -1 & 0 & 0 \end{pmatrix} \cdot \begin{pmatrix} I_R^m \\ I_L^n \\ I_X^{m,n} \\ I_D^{m,n} \end{pmatrix}. \tag{D9}$$

However, this is not the final device matrix since the measured intensities are composed of the four polarization components $I_0^{m,n} = (I_R^m, I_L^n, I_X^{m,n}, I_D^{m,n})^T$ and the background intensities $B_0^{m,n} = (B_R^m, B_L^n, B_X^{m,n}, B_D^{m,n})^T$, which consist of transmitted light not modulated by the metasurfaces as well as cross-talk between the different metasurfaces structures. Let us assume there is also a linear relationship among the four polarization components and the background intensities:

$$\begin{pmatrix} B_R^m \\ B_L^n \\ B_X^{m,n} \\ B_D^{m,n} \end{pmatrix} = N^{m,n} \cdot \begin{pmatrix} I_R^m \\ I_L^n \\ I_X^{m,n} \\ I_D^{m,n} \end{pmatrix}, \tag{D10}$$

where $N^{m,n}$ is a 4×4 matrix. Therefore, the relationship between the four polarization components and the measured intensities $I_{m,n} = (I_1^{m,n}, I_2^{m,n}, I_3^{m,n}, I_4^{m,n})^T$ can be expressed as

$$\begin{pmatrix} I_1^{m,n} \\ I_2^{m,n} \\ I_3^{m,n} \\ I_4^{m,n} \end{pmatrix} - \begin{pmatrix} B_R^m \\ B_L^n \\ B_X^{m,n} \\ B_D^{m,n} \end{pmatrix} = \begin{pmatrix} I_R^m \\ I_L^n \\ I_X^{m,n} \\ I_D^{m,n} \end{pmatrix}, \tag{D11}$$

where $I_{m,n} = (I_1^{m,n}, I_2^{m,n}, I_3^{m,n}, I_4^{m,n})^T$ represents the intensities measured at the four focusing spots. From Eqs. (D9)–(D11), the relationship between the higher-order Stokes parameters and the final device matrix $D^{m,n}$ can be derived as

$$\begin{aligned} S_{m,n} &= M^{m,n} \cdot I_0^{m,n} = M^{m,n} \cdot (E + N^{m,n})^{-1} \cdot I_{m,n} \\ &= D^{m,n} \cdot I_{m,n}, \end{aligned} \tag{D12}$$

where $S_{m,n} = (S_0^{m,n}, S_1^{m,n}, S_2^{m,n}, S_3^{m,n})^T$ represents the Stokes parameters and E is a 4×4 unit matrix. From Eq. (D12), the final device matrix $D^{m,n}$ can be calculated by using $D^{m,n} = S_{m,n} \cdot \mathrm{pinv}(I_{m,n})$. For our designed metadevice, the process to determine the final device matrix $D^{m,n}$ is defined as the device calibration process, in which four standard polarization states and their corresponding measured intensities are utilized to calculate the values of final device matrix $D^{m,n}$. By utilizing the simulated intensities in Table 1 and Table 2, the final device matrix $D^{m,n}$ for these two cases is calculated as

$$D^{0,0} = \begin{bmatrix} 0.1703 & 0.1708 & 0.0151 & 0.0003 \\ -0.2341 & -0.2364 & 0.3573 & 0.0043 \\ -0.2267 & -0.2241 & -0.0136 & 0.3582 \\ 0.1834 & -0.2191 & -0.0018 & 0.0285 \end{bmatrix}, \tag{D13}$$

Table 3. Reconstructing the Stokes Parameters on $HOPS_{0,0}$ Using the Metadevice with a-Si on Silica Substrate Configuration

Stokes Parameters $(S_0^{0,0}, S_1^{0,0}, S_2^{0,0}, S_3^{0,0})$	Simulated Intensities (%) $(I_1^{0,0}, I_2^{0,0}, I_3^{0,0}, I_4^{0,0})$	Reconstructed Stokes Parameters (Simulated)	Error
(1,0,0,1)	(8.863,0.635,4.879,4.271)	(1.0000,0.0000,0.0000,0.0000)	0
(1,0,0,−1)	(0.669,8.994,4.392,4.623)	(1.0000,0.0000,0.0000,−1.0000)	0
(1,1,0,0)	(4.925,4.982,7.322,4.342)	(1.0000,1.0000,0.0000,0.0000)	0
(1,0,1,0)	(4.910,4.648,4.576,6.782)	(1.0000,0.0000,1.0000,0.0000)	0
(1,0,−1,0)	(4.623,4.981,4.695,2.113)	(1.0001,−0.0002,−0.9998,0.0001)	0.0002
(1,−1,0,0)	(4.607,4.647,1.950,4.533)	(1.0000,−0.9996,0.0005,−0.0000)	0.0002
(1,0,0.866,0.5)	(2.842,6.760,4.462,6.557)	(1.0000,−0.0000,0.8660,0.5000)	0
(1,0,0.866,−0.5)	(6.939,2.581,4.706,6.381)	(1.0000,0.0001,0.8659,−0.4999)	0.0001

Table 4. Reconstructing the Stokes Parameters on $HOPS_{1,-1}$ Using the Metadevice with a-Si on Silica Substrate Configuration

Stokes Parameters $(S_0^{1,-1}, S_1^{1,-1}, S_2^{1,-1}, S_3^{1,-1})$	Simulated Intensities (%) $(I_1^{1,-1}, I_2^{1,-1}, I_3^{1,-1}, I_4^{1,-1})$	Reconstructed Stokes Parameters (Simulated)	Error
(1,0,0,1)	(9.628,0.719,5.265,4.607)	(1.0000,0.0000,0.0000,0.0000)	0
(1,0,0,−1)	(0.752,9.763,4.724,4.927)	(1.0000,0.0000,0.0000,−1.0000)	0
(1,1,0,0)	(5.009,5.048,2.773,3.345)	(1.0000,1.0000,0.0000,0.0000)	0
(1,0,1,0)	(5.179,5.240,3.324,2.897)	(1.0000,0.0000,1.0000,0.0000)	0
(1,0,−1,0)	(5.200,5.242,6.667,6.638)	(0.9999,−0.0013,−0.9999,−0.0001)	0.0004
(1,−1,0,0)	(5.370,5.433,7.217,6.190)	(0.9998,−1.0003,−0.0008,−0.0000)	0.0003
(1,0,0.866,0.5)	(7.400,2.979,3.683,3.067)	(1.0000,−0.0004,0.8667,0.5001)	0.0002
(1,0,0.866,−0.5)	(2.980,7.503,6.307,6.468)	(1.0000,0.0003,0.8671,−0.5001)	0.0004

$$D^{1,-1} = \begin{bmatrix} 0.1125 & 0.1128 & 0.0557 & -0.0408 \\ 0.1257 & 0.1363 & -0.7729 & 0.5650 \\ 0.1032 & 0.0922 & 0.6833 & -0.8306 \\ 0.1328 & -0.1399 & -0.0207 & 0.0251 \end{bmatrix}. \tag{D14}$$

Then, the designed metadevice is capable of accurately resolving the polarization states by calculating the higher-order Stokes parameters from Eq. (D11).

APPENDIX E: METADEVICE WITH A-SI ON SILICA SUBSTRATE CONFIGURATION

In the main text, we choose an all-silicon configuration and demonstrate a metadevice for fully resolving arbitrary beams on a HOPS. The all-silicon configuration is selected for its simpler fabrication procedure (requires no additional film deposition during the fabrication procedure) compared with the a-Si on silica substrate configuration. Actually, identical functionality could be achieved for our proposed metadevice with a-Si on silica substrate configuration. To show that, the all-silicon metadevice is replaced with a-Si on silica substrate configuration (the refractive indexes of a-Si and silica are set as 3.7 and 1.46, respectively). The unit cell consists of an a-Si nanoblock placed on a silica substrate. The lattice constant is $P = 600$ nm, and the height of the nanoblock is $h = 800$ nm. With the same strategy, we repeated all the optimization processes and accomplished the same functionalities (resolving different beams on $HOPS_{0,0}$ and $HOPS_{1,-1}$). The intensity profiles for the metadevice with a-Si on the silica substrate configuration are identical with those in the main text and hence are not shown here. The corresponding simulated focusing efficiencies and reconstructed Stokes parameters are shown in Tables 3 and 4, respectively. For both cases, the reconstructed Stokes parameters show good agreement with the original ones. From the four tables, one can find that the total intensity of the a-Si on silica substrate configuration is slightly larger than that of the all-silicon configuration. However, the metadevice based on these two configurations shows approximate performance. Therefore, we choose the all-silicon configuration for its simpler fabrication procedure.

Funding. Guangdong Major Project of Basic and Applied Basic Research (2020B0301030009); National Key Research and Development Program of China (2018YFB1801801); National Natural Science Foundation of China (U1701661, 61935013, 61975133, 11604218, 11774240, 11947017); Natural Science Foundation of Guangdong Province (2016A030312010, 2020A1515011185); Leadership of Guangdong Province Program (00201505); Science and Technology Innovation Commission of Shenzhen grants Shenzhen Peacock Plan (JCYJ20180507182035270, KQJSCX20170727100838364, KQTD20170330110444030, ZDSYS201703031605029, JCYJ20200109114018750, JCYJ20180305125418079); Shenzhen University (2019075).

Acknowledgment. H. Wang acknowledges financial support from the Ministry of Education of Singapore (MOE2016-T2-1-052).

Disclosures. The authors declare no conflicts of interest.

REFERENCES

1. M. Born and E. Wolf, *Principles of Optics*, 7th ed. (Cambridge University, 1999).
2. R. M. A. Azzam and N. M. Bashara, *Ellipsometry and Polarized Light* (North-Holland, 1977).
3. G. Milione, H. I. Sztul, D. A. Nolan, and R. R. Alfano, "Higher-order Poincaré sphere, Stokes parameters, and the angular momentum of light," Phys. Rev. Lett. **107**, 053601 (2011).
4. G. Milione, S. Evans, D. A. Nolan, and R. R. Alfano, "Higher-order Pancharatnam–Berry phase and the angular momentum of light," Phys. Rev. Lett. **108**, 190401 (2012).
5. X. Yi, Y. Liu, X. Ling, X. Zhou, Y. Ke, H. Luo, S. Wen, and D. Fan, "Hybrid-order Poincaré sphere," Phys. Rev. A **91**, 023801 (2015).
6. Z. Liu, Y. Liu, Y. Ke, Y. Liu, W. Shu, H. Luo, and S. Wen, "Generation of arbitrary vector vortex beams on hybrid-order Poincaré sphere," Photon. Res. **5**, 15–21 (2017).
7. D. Naidoo, F. S. Roux, A. Dudley, I. Litvin, B. Piccirillo, L. Marrucci, and A. Forbes, "Controlled generation of higher-order Poincaré sphere beams from a laser," Nat. Photonics **10**, 327–332 (2016).
8. Z. H. Jiang, L. Kang, T. Yue, H. Xu, Y. Yang, Z. Jin, C. Yu, W. Hong, D. H. Werner, and C. Qiu, "A single noninterleaved metasurface for high-capacity and flexible mode multiplexing of higher-order Poincaré sphere beams," Adv. Mater. **32**, 1903983 (2020).
9. A. F. Abouraddy and K. C. Toussaint, "Three-dimensional polarization control in microscopy," Phys. Rev. Lett. **96**, 153901 (2006).
10. X. Xie, Y. Chen, K. Yang, and J. Zhou, "Harnessing the point spread function for high-resolution far-field optical microscopy," Phys. Rev. Lett. **113**, 263901 (2014).
11. J. Ng, Z. Lin, and C. T. Chan, "Theory of optical trapping by an optical vortex beam," Phys. Rev. Lett. **104**, 103601 (2010).
12. B. K. Singh, H. Nagar, Y. Roichman, and A. Arie, "Particle manipulation beyond the diffraction limit using structured super-oscillating light beams," Light Sci. Appl. **6**, e17050 (2017).
13. C. H. Bennett and D. P. DiVincenzo, "Quantum information and computation," Nature **404**, 247–255 (2000).
14. N. Bozinovic, Y. Yue, Y. Ren, M. Tur, P. Kristensen, H. Huang, A. E. Willner, and S. Ramachandran, "Terabit-scale orbital angular momentum mode division multiplexing in fibers," Science **340**, 1545–1548 (2013).
15. J. Fang, Z. Xie, T. Lei, C. Min, L. Du, Z. Li, and X. Yuan, "Spin-dependent optical geometric transformation for cylindrical vector beam multiplexing communication," ACS Photon. **5**, 3478–3484 (2018).
16. R. M. Matchko and G. R. Gerhart, "High-speed imaging chopper polarimetry," Opt. Eng. **47**, 016001 (2008).
17. H. G. Berry, G. Gabrielse, and A. E. Livingston, "Measurement of the Stokes parameters of light," Appl. Opt. **16**, 3200–3205 (1977).
18. N. Yu, P. Genevet, M. A. Kats, F. Aieta, J. P. Tetienne, F. Capasso, and Z. Gaburro, "Light propagation with phase discontinuities: generalized laws of reflection and refraction," Science **334**, 333–337 (2011).
19. N. Yu and F. Capasso, "Flat optics with designer metasurfaces," Nat. Mater. **13**, 139–150 (2014).
20. S. Rubin and Y. Fainman, "Nonlinear, tunable, and active optical metasurface with liquid film," Adv. Photon. **1**, 066003 (2019).
21. W. Liu, Z. Li, H. Cheng, C. Tang, J. Li, S. Zhang, S. Chen, and J. Tian, "Metasurface enabled wide-angle Fourier lens," Adv. Mater. **30**, 1706368 (2018).
22. S. Wang, P. C. Wu, V. Su, Y. Lai, M. Chen, H. Y. Kuo, B. H. Chen, Y. H. Chen, T. Huang, J. Wang, R. Lin, C. Kuan, T. Li, Z. Wang, S. Zhu, and D. P. Tsai, "A broadband achromatic metalens in the visible," Nat. Nanotechnol. **13**, 227–232 (2018).
23. H. Yang, G. Cao, K. Ou, G. Li, and X. Chen, "Broadband spin-driven anomalous surface plasmon polariton steering via V-shaped aperture metasurfaces," Adv. Theory Simul. **2**, 1800167 (2019).
24. L. Du, Z. Xie, G. Si, A. Yang, C. Li, J. Lin, G. Li, H. Wang, and X. Yuan, "On-chip photonic spin Hall lens," ACS Photon. **6**, 1840–1847 (2019).
25. N. A. Rubin, G. D'Aversa, P. Chevalier, Z. Shi, W. T. Chen, and F. Capaso, "Matrix Fourier optics enables a compact full-Stokes polarization camera," Science **365**, eaax1839 (2019).
26. Z. Shen, S. Zhou, X. Li, S. Ge, P. Chen, W. Hu, and Y. Lu, "Liquid crystal integrated metalens with tunable chromatic aberration," Adv. Photon. **2**, 036002 (2020).
27. K. Ou, F. Yu, G. Li, W. Wang, A. E. Miroshnichenko, L. Huang, P. Wang, T. Li, Z. Li, X. Chen, and W. Lu, "Mid-infrared polarization-controlled broadband achromatic metadevice," Sci. Adv. **6**, eabc0711 (2020).
28. R. C. Devlin, A. Ambrosio, N. A. Rubin, J. P. B. Mueller, and F. Capasso, "Arbitrary spin-to-orbital angular momentum conversion of light," Science **358**, 896–901 (2017).
29. F. Yue, D. Wen, C. Zhang, B. D. Gerardot, W. Wang, S. Zhang, and X. Chen, "Multichannel polarization-controllable superpositions of orbital angular momentum states," Adv. Mater. **29**, 1603838 (2017).
30. Y. Bao, J. Ni, and C. W. Qiu, "A minimalist single-layer metasurface for arbitrary and full control of vector vortex beams," Adv. Mater. **32**, 1905659 (2020).
31. J. P. B. Mueller, N. A. Rubin, R. C. Devlin, B. Groever, and F. Capasso, "Metasurface polarization optics: independent phase control of arbitrary orthogonal states of polarization," Phys. Rev. Lett. **118**, 113901 (2017).
32. S. M. Kamali, E. Arbabi, A. Arbabi, Y. Horie, M. Faraji-Dana, and A. Faraon, "Angle-multiplexed metasurfaces: encoding independent wavefronts in a single metasurface under different illumination angles," Phys. Rev. X **7**, 041056 (2017).
33. H. Ren, G. Briere, X. Fang, P. Ni, R. Sawant, S. Héron, S. Chenot, S. Vézian, B. Damilano, V. Brändli, S. A. Maier, and P. Genevet, "Metasurface orbital angular momentum holography," Nat. Commun. **10**, 2986 (2019).
34. X. Fang, H. Ren, and M. Gu, "Orbital angular momentum holography for high-security encryption," Nat. Photonics **14**, 102–108 (2020).
35. F. Afshinmanesh, J. S. White, W. Cai, and M. L. Brongersma, "Measurement of the polarization state of light using an integrated plasmonic polarimeter," Nanophotonics **1**, 125–129 (2012).
36. A. Pors, M. G. Nielsen, and S. I. Bozhevolnyi, "Plasmonic metagratings for simultaneous determination of Stokes parameters," Optica **2**, 716–723 (2015).
37. J. P. B. Mueller, K. Leosson, and F. Capasso, "Ultracompact metasurface in-line polarimeter," Optica **3**, 42–47 (2016).
38. S. Wei, Z. Yang, and M. Zhao, "Design of ultracompact polarimeters based on dielectric metasurfaces," Opt. Lett. **42**, 1580–1583 (2017).
39. Z. Yang, Z. Wang, Y. Wang, X. Feng, M. Zhao, Z. Wan, L. Zhu, J. Liu, Y. Huang, J. Xia, and M. Wegener, "Generalized Hartmann-Shack array of dielectric metalens sub-arrays for polarimetric beam profiling," Nat. Commun. **9**, 4607 (2018).
40. K. Lee, H. Yun, S. E. Mun, G. Y. Lee, J. Sung, and B. Lee, "Ultracompact broadband plasmonic polarimeter," Laser Photon. Rev. **12**, 1700297 (2018).
41. P. C. Wu, J. W. Chen, C. W. Yin, Y. C. Lai, T. L. Chung, C. Y. Liao, B. H. Chen, K. W. Lee, C. J. Chuang, C. M. Wang, and D. P. Tsai, "Visible metasurfaces for on-chip polarimetry," ACS Photon. **5**, 2568–2573 (2018).
42. X. Zhang, S. Yang, W. Yue, Q. Xu, C. Tian, X. Zhang, E. Plum, S. Zhang, J. Han, and W. Zhang, "Direct polarization measurement using a multiplexed Pancharatnam–Berry metahologram," Optica **6**, 1190–1198 (2019).
43. J. Chen, X. Chen, T. Li, and S. Zhu, "On-chip detection of orbital angular momentum beam by plasmonic nanogratings," Laser Photon. Rev. **12**, 1700331 (2018).
44. H. Yang, Z. Chen, Q. Liu, Q. Y. Hu, and H. Duan, "Near-field orbital angular momentum generation and detection based on spin-orbit interaction in gold metasurfaces," Adv. Theory Simul. **2**, 1900133 (2019).
45. F. Feng, G. Si, C. Min, X. Yuan, and M. Somekh, "On-chip plasmonic Spin-Hall nanograting for simultaneously detecting phase and polarization singularities," Light Sci. Appl. **9**, 95 (2020).
46. S. Zhang, P. Huo, W. Zhu, C. Zhang, P. Chen, M. Liu, L. Chen, H. Lezec, A. Agrawal, Y. Lu, and T. Xu, "Broadband detection of multiple

spin and orbital angular momenta via dielectric metasurface," Laser Photon. Rev. **14**, 2000062 (2020).
47. Q. Fan, W. Zhu, Y. Liang, P. Huo, C. Zhang, A. Agrawal, K. Huang, X. Luo, Y. Lu, C. Qiu, H. Lezec, and T. Xu, "Broadband generation of photonic spin-controlled arbitrary accelerating light beams in the visible," Nano Lett. **19**, 1158–1165 (2018).
48. G. Ding, K. Chen, X. Luo, J. Zhao, T. Jiang, and Y. Feng, "Dual-helicity decoupled coding metasurface for independent spin-to-orbital angular momentum conversion," Phys. Rev. A **11**, 044043 (2019).
49. L. Huang, X. Song, B. Reineke, T. Li, X. Li, J. Liu, S. Zhang, Y. Wang, and T. Zentgraf, "Volumetric generation of optical vortices with metasurfaces," ACS Photon. **4**, 338–346 (2017).